Assessing the reliability of the modified three-component spatial autocorrelation technique

Andreas Köhler,[1] Matthias Ohrnberger,[1] Frank Scherbaum,[1] Marc Wathelet[2] and Cecile Cornou[2,3]

[1]*Institut für Geowissenschaften, Universität Potsdam, Karl-Liebknecht-Str.* 24, *Haus* 27, 14476 *Golm, Germany. E-mail: akoehler@uni-potsdam.de*
[2]*LGIT (Laboratoire de Geophysique Interne et Tectonophysique), Université Joseph Fourier,* 1381, *rue de la Piscine* - BP 53, 38041 *Grenoble cedex* 1, *France*
[3]*IRD (Institut de recherche et de developpement), Paris, France*

SUMMARY

Analysis of seismic ambient vibrations is becoming a widespread approach to estimate sub-surface shear wave velocity profiles. However, the common restriction to vertical component wavefield data does not allow investigations of Love wave dispersion and the partitioning between Rayleigh and Love waves. In this study we extend the modified spatial autocorrelation technique (MSPAC) to three-component analysis (3c-MSPAC). By determination of Love wave dispersion curves, this technique provides additional information for the determination of shear wave velocity–depth profiles. Furthermore, the relative fraction of Rayleigh waves in the total portion of surface waves on the horizontal components is estimated. Tests of the 3c-MSPAC method are presented using synthetic ambient vibration waveform data. Different types of surface waves are simulated as well as different modes. In addition, different spatial distributions of sources are used. We obtain Rayleigh and Love wave dispersion curves for broad frequency bands in agreement with the models used for waveform simulation. The same applies for the relative fraction of Rayleigh waves. Dispersion curves are observed at lower frequencies for Love waves than for Rayleigh waves. While 3c-MSPAC has clear advantages for determination of Love waves velocities, 3c-MSPAC and conventional vertical frequency–wavenumber analysis complement each other in estimating the Rayleigh wave dispersion characteristics. Inversions of the dispersion curves for the shear wave velocity–depth profile show that the use of Love wave velocities confirms the results derived from Rayleigh wave velocities. In the presence of higher mode surface waves, Love waves even can improve results. Application of 3c-MSPAC to ambient vibration data recorded during field measurements (Pulheim, Germany) show dominance of Love waves in the wavefield. Existing shear wave profiles for this site are consistent with models obtained from inversion of Rayleigh and Love wave dispersion curves.

Key words: seismic array, seismic noise, seismology, surface waves.

1 INTRODUCTION

Knowledge about the subsurface elastic properties is important for prediction of local site effects on seismic wave amplitudes which is crucial for seismic hazard assessment (Hartzell *et al.* 1996; Yamanaka 1998). Recordings of ambient vibrations using seismometer arrays and single stations can be used to obtain such information (e.g. Milana *et al.* 1996; Ohmachi & Umezono 1998; Bard 1998). That approach is cost effective and easily realized and has therefore become increasingly popular in recent years. The ambient vibration analysis is a suitable alternative for urban areas as well as for regions where seismicity is too low for empirical site effect characterization based on earthquake recordings. Evidenced by many authors in the past, it is commonly assumed that surface waves dominate the ambient vibration wavefield (see e.g. Asten 1976; Lachet & Bard 1994; Cornou & Bard 2003; Bonnefoy-Claudet *et al.* 2004, 2005). Then, Rayleigh wave ellipticities can be derived from single-station 3c recordings using spectral ratios of the horizontal and vertical (H/V) displacement field (e.g. Arai & Tokimatsu 2000). Furthermore, surface wave dispersion curves can be determined by means of array methods (Aki 1957; Lacoss *et al.* 1969; Asten & Henstridge 1984; Horike 1985; Tokimatsu & Miyadera 1992; Tokimatsu 1997). This allows inversion for the 1-D velocity structure below the station array (Malagnini *et al.* 1995; Herrmann 2001; Scherbaum *et al.* 2003; Wathelet *et al.* 2005; Parolai *et al.* 2005).

Frequency–wavenumber analysis (FK: Lacoss *et al.* 1969) and the spatial autocorrelation method (SPAC: Aki 1957) are the most commonly employed array techniques. FK analysis is in general applicable to vertical and both horizontal wavefield components. SPAC was

also originally introduced as a three-component method. Both methods can be applied due to the fact that Rayleigh and Love waves can be separated using the vertical, the radial (both Rayleigh) and the transverse (Love) component. However, in the case of ambient vibrations we are often dealing with unknown and/or multiple source directions. Therefore, mixing of Rayleigh and Love waves occurs on the horizontal components leading to ambiguous results. Thus, the majority of the ambient vibration studies make only use of the vertical component wavefield with the goal to estimate Rayleigh wave dispersion curves. However, Love wave phase velocities are of particular interest because the combined use of Rayleigh and Love wave dispersion curves reduces non-uniqueness during inversion for the shear wave velocity structure. Furthermore, the estimation of the relative fraction of Rayleigh and Love waves can provide further insight into the characteristics of ambient vibrations.

A few authors applied FK analysis to three-component ambient vibration data (e.g. Tokimatsu 1997; DiGiulio *et al.* 2006). Provided that the direction of wave propagation is known or only Love waves are present, the Love wave dispersion curve can be additionally determined using FK analysis. Tokimatsu (1997) found evidences for a dominance of Love waves in ambient vibration data. Unlike FK, the three-component SPAC method allows to determine dispersion characteristics of Love and Rayleigh waves as well as their respective relative portion in the horizontal ground motion. Using SPAC, no additional assumptions concerning directions of wave propagation are required. Aki (1957) analysed ambient noise in an urban area to test 3c-SPAC. He also reported a dominance of Love waves on the horizontal components. Métaxian *et al.* (1997), Chouet *et al.* (1998) and Saccorotti *et al.* (2003) applied the 3c-SPAC method to signals of volcanic tremors. They also suggest a high portion or at least a slight preponderance of Love waves. However, in general the partitioning between Rayleigh and Love waves is still under debate (see reviews of Bonnefoy-Claudet *et al.* 2004, 2005). We refer also to Okada (2003) for a further discussion about three-component ambient vibration analysis in general.

A couple of modifications and extensions of the traditional SPAC technique have been developed since Aki (1957). Ohori *et al.* (2002) for example introduced an extension to more complex array layouts (ESAC). Very recently Cho *et al.* (2006) presented an extended three-component array method including Aki's 3c-SPAC approach. In contrast to FK methods, regular array configurations are required to utilize the traditional SPAC method. Bettig *et al.* (2001) developed the modified vertical SPAC method (MSPAC) which allows arbitrary array layouts.

Between 2001 and 2004 the European SESAME project (Site EffectS assessment using AMbient Excitations, see e.g. Bard 2004) was carried out in order to propose user guidelines and recommendations for the application of different ambient vibration analysis techniques (e.g. vertical MSPAC). This paper presents the extension of the vertical MSPAC method to three-component analysis (3c-MSPAC). Applying 3c-MSPAC we determined Rayleigh and Love wave dispersion curves from synthetic waveform data which are generated by simulated ambient vibrations. In order to test its reliability, we compare the results with the theoretical dispersion curves and results of FK analysis. Finally, we invert for the shear wave velocity-depth profiles.

In a second step we apply 3c-MSPAC to real data of ambient vibration array measurements in the Lower Rhine Embayment. The Lower Rhine Embayment (LRE) in western Germany forms the northern part of the Central European tertiary rift system (Fig. 1). Due to still ongoing subsidental movement on NW-SE striking normal faults, the LRE is one of the most seismically active regions within Central Europe (e.g. the 1992 magnitude 5.9 Roermond earthquake). Since the region is a densely populated area with large cities like Cologne (population ≈1 million), seismic hazard analysis requires reliable subsurface models. Several ambient vibration studies were carried out in the past in order to investigate the basin filled with Quaternary and Tertiary soft sediments. Ibs Van Seht & Wohlenberg (1999), Parolai *et al.* (2002) and Hinzen *et al.* (2004) used H/V spectral ratios at different sites in the LRE to estimate the depth of the sediment–bedrock interface as well as the subsurface shear wave velocities. The city of Pulheim located close to Cologne (Fig. 1) was the target site for several studies in the past and, therefore, is a relative well explored site in the LRE. In particular, analysis of local earthquakes (Ohrnberger *et al.* 2004a), joint inversion of H/V spectral ratios and dispersion curves (Scherbaum *et al.* 2003; Parolai *et al.* 2005; Picozzi *et al.* 2005) as well as comparison of vertical MSPAC with different vertical FK techniques (Ohrnberger *et al.* 2004b) were performed to investigate the local subsurface velocity structure.

2 THEORY

The spatial autocorrelation function Φ describes the similarity between the seismograms $u(t, x)$ and $u(t, x + \varepsilon)$ recorded at receiver positions x and $x + \varepsilon$ at time t. In one dimension, we calculate Φ as a function of distance ε between the receivers for a specified time window T:

$$\Phi(\varepsilon) = \langle \Phi(\varepsilon, t) \rangle_t = \frac{1}{T} \cdot \int_0^T u(x, t) \cdot u(x + \varepsilon, t) \cdot dt. \tag{1}$$

By bandpass filtering with a narrow passband before correlation, eq. (1) becomes frequency-dependent ($\Phi(\varepsilon) = \Phi(\varepsilon, \omega)$). Assuming a stochastic wavefield that is stationary in time and space, the spatial autocorrelation depends directly on the unknown phase velocity $c(\omega)$ of the seismic wave (Aki 1957).

For two dimensions ($x - y$ plane) ε in (1) can be rewritten via polar coordinates r (distance between receivers) and φ (angle between x-axis and connecting line) as $\varepsilon = r \cdot \cos(\theta - \varphi)$. θ is the angle between a single horizontal wave propagation direction and the x-axis. If θ and thus ε are unknown, $c(\omega)$ cannot be estimated from the autocorrelation. However, Aki (1957) showed that a directional-independent averaged autocorrelation coefficient $\overline{\rho}(r, \omega)$ can be obtained by integrating the autocorrelation function over φ and afterwards
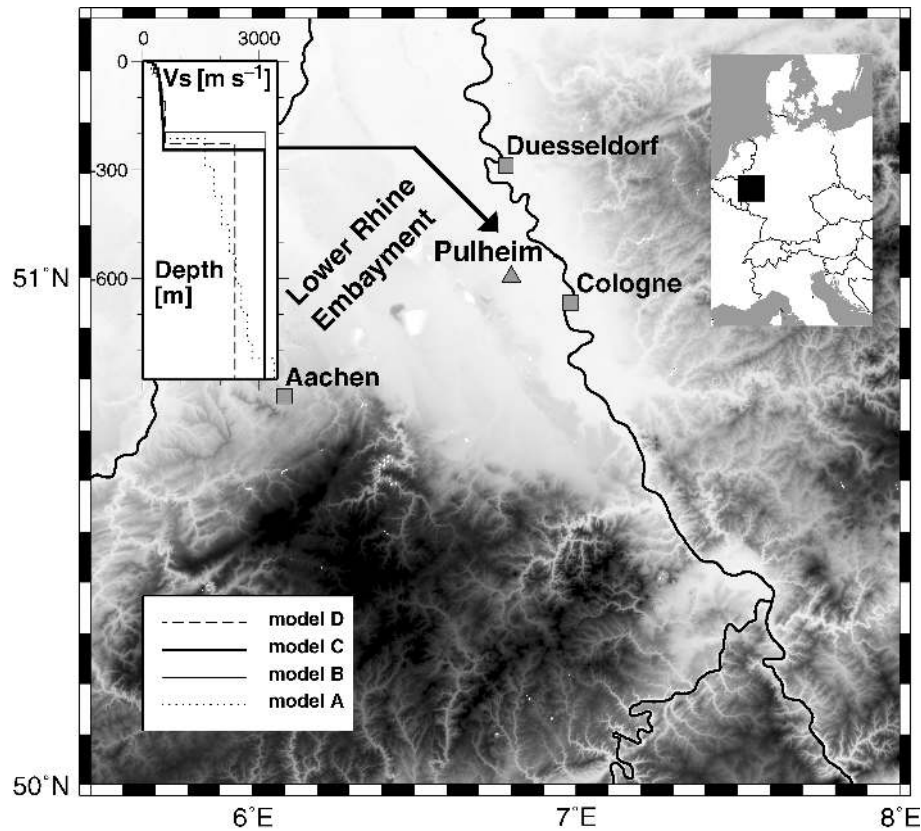
Figure 1. Elevation map and location (top right) of the Lower Rhine Embayment (NW Germany). The triangle indicates the location of the array measurements (Pulheim). Top left: shear velocity models for the Pulheim site (for the legend see the box at the bottom): model A (Brüstle & Stange 1999; Brüstle *et al.* 2000), model B (Scherbaum *et al.* 2003), model C (Ohrnberger *et al.* 2004a) and model D (Parolai *et al.* 2005; Picozzi *et al.* 2005).

normalizing it. This leads to a zero order Bessel function $J_0(\omega, r, c(\omega))$:

$$\overline{\rho}(r, \omega) = \frac{\int_0^{2\pi} \Phi(r, \varphi, \omega) d\varphi}{\int_0^{2\pi} \Phi(0, \varphi, \omega) d\varphi} = J_0\left(\frac{\omega \cdot r}{c(\omega)}\right). \tag{2}$$

Integration over φ represents averaging of the autocorrelation coefficients for station pairs with equal distances but different azimuths. For two stations, integration over θ represents averaging over wavefields propagating in different directions θ. Note that both approaches are equivalent. In practice, multiple source directions often occur in ambient vibration wavefields. Thus, using only a few (at least two) receivers, the integration over θ implies that an application of SPAC to ambient vibrations is very promising (see e.g. Morikawa *et al.* 2004; Chaves-Garcia *et al.* 2005). Another recent approach which utilizes this observation is cross-correlation of global or regional long term ambient noise data at two seismic broad-band stations. This allows to estimate the Green's functions of the medium between the receivers (Shapiro *et al.* 2005).

For a superposition of n stationary waves with different phase velocities Aki (1957) showed that the measured autocorrelation coefficient $\overline{\rho}$ can be decomposed into the autocorrelation coefficient $\overline{\rho}_n$ of each wave:

$$\overline{\rho}(r, \omega) = \sum_n \frac{P_n(\omega)}{P(\omega)} \cdot \overline{\rho}_n(r, \omega), \tag{3}$$

where $P_n(\omega)$ is the power spectrum density for the nth wave and $P(\omega)$ the power spectrum density of the whole wavefield (see also Tokimatsu 1997).

Furthermore, the averaged autocorrelation coefficients of the radial $\overline{\rho}_r$ and tangential component $\overline{\rho}_t$ (with respect to the connecting line between two receivers) can be expressed as the sum of two Bessel functions of zero and second order (see Aki 1957). Assuming only single-mode Rayleigh and Love waves (two summands in 3), the averaged autocorrelation coefficients can be determined (Bettig *et al.* 2001):

$$\overline{\rho}_z(r, \omega) = J_0(w_R), \tag{4}$$

$$\overline{\rho}_r(r, \omega) = \alpha(\omega) \cdot \{J_0(w_R) - J_2(w_R)\} + (1 - \alpha(\omega)) \cdot \{J_0(w_L) + J_2(w_L)\}, \tag{5}$$

$$\overline{\rho}_t(r, \omega) = \alpha(\omega) \cdot \{J_0(w_R) + J_2(w_R)\} + (1 - \alpha(\omega)) \cdot \{J_0(w_L) - J_2(w_L)\}, \tag{6}$$

where $w_R = \omega \cdot r/C_R(\omega)$, $w_L = \omega \cdot r/C_L(\omega)$ and $\overline{\rho}_z$ is the vertical autocorrelation coefficient.

Note that azimuthal averaging of the autocorrelation function must be done before normalization for radial and tangential component (see eq. 2). Otherwise identical expressions for the vertical and horizontal autocorrelation coefficients are obtained.

Formulae (4)–(6) allow to determine the Rayleigh wave phase velocity $C_R(\omega)$, the Love wave phase velocity $C_L(\omega)$, and the relative fraction of Rayleigh $\alpha(\omega) = P_R/(P_R + P_L)$, and Love waves $(1 - \alpha(\omega))$ on the horizontal components of the wavefield. P_R and P_L represent the spectral power of Rayleigh and Love waves, respectively, on the horizontal components (see P_n in eq. 3). Due to aliasing and lack of resolution, the range where the arguments w_R and w_L can be determined uniquely from the value of the Bessel function is restricted (Okada 2003). Using different radii r changes the shape of the Bessel function and extends the usable frequency band to a wider range.

Eq. (2) implies that one or several pairs of stations with equal inter station-distances r are needed for the integration over φ. Therefore, circular (Aki 1957) or in general regular (Ohori *et al.* 2002) array geometries are required for SPAC in contrast to FK analysis. However, the realization of regular arrays is difficult or impracticable in urban areas where ambient vibration measurements are carried out mostly. Bettig *et al.* (2001) therefore introduced the modified spatial autocorrelation method for the vertical wavefield component (MSPAC). MSPAC makes the autocorrelation technique applicable for arbitrary array configurations. For this purpose the co-array is defined as the set of all possible combinations of two array stations (Haubrich 1968). Following Bettig *et al.* (2001) it can be divided into rings. The total number and the width of each ring depends on the azimuthal and radial distribution of the station pairs forming the co-array. An azimuthal and radial integration is introduced. It corresponds to averaging over all autocorrelation coefficients situated within a particular ring. Assuming again only single-mode surface waves, the averaged vertical autocorrelation coefficient $\overline{\rho_{z,k}}$ of the kth ring writes (Bettig *et al.* 2001):

$$\overline{\rho_{z,k}}(\omega) = \frac{2}{r_2^2 - r_1^2} \cdot \frac{C_R}{\omega} \cdot [r_2 \cdot J_1(w_R) - r_1 \cdot J_1(w_R)] = \frac{2}{r_2^2 - r_1^2} \cdot \frac{C_R}{\omega} \cdot [r \cdot J_1(w_R)]_{r_1}^{r_2}. \tag{7}$$

In (7) r_1 and r_2 ($r_1 < r_2$) define the width of the kth ring.

In this study, we extend the MSPAC method to the three components of the wavefield. In addition to (7) the corresponding radial and tangential autocorrelation coefficients $\overline{\rho_{r,k}}$ and $\overline{\rho_{t,k}}$, respectively, are given as:

$$\overline{\rho_{r,k}}(\omega) = \frac{4}{r_2^2 - r_1^2} \left\{ \frac{\alpha \cdot C_R}{\omega} \cdot \left(\frac{C_R}{\omega} \cdot [J_0(w_R)]_{r_1}^{r_2} + [r \cdot J_1(w_R)]_{r_1}^{r_2} \right) - \frac{(1 - \alpha)C_L^2}{\omega^2} \cdot [J_0(w_L)]_{r_1}^{r_2} \right\}, \tag{8}$$

$$\overline{\rho_{t,k}}(\omega) = \frac{4}{r_2^2 - r_1^2} \left\{ \frac{(-\alpha) \cdot C_R^2}{\omega^2} \cdot [J_0(w_R)]_{r_1}^{r_2} + \frac{(1 - \alpha)C_L}{\omega} \cdot \left(\frac{C_L}{\omega} \cdot [J_0(w_L)]_{r_1}^{r_2} + [r \cdot J_1(w_L)]_{r_1}^{r_2} \right) \right\}, \tag{9}$$

where $C_L = C_L(\omega)$, $C_R = C_R(\omega)$, and $\alpha = \alpha(\omega)$.

For a co-array divided into N rings, we now have $3N$ data points for each frequency in order to estimate the three unknowns $C_R(\omega)$, $C_L(\omega)$ and $\alpha(\omega)$.

3 PROCESSING AND GRID SEARCH

We compute the autocorrelation function (1) for each station pair of the receiver array. The frequency dependence is obtained by applying a narrow bandpass filter for 70 central frequencies f_c. Lower and upper limits of the passband correspond to $0.9 \cdot f_c$ and $1.1 \cdot f_c$, respectively. We use central frequencies linearly distributed on a logarithmic scale between 0.5 and 2.5 Hz. A sliding window analysis is employed. Each time segment has a length depending linearly upon the period considered. In order to calculate radial and tangential autocorrelations, we have to rotate the horizontal seismogram components (N,E) with respect to the orientation of the receiver pair considered.

The azimuthal and radial averaging of the autocorrelation function (numerator in 2) and normalization factors (autocorrelations at $r = 0$, denominator in 2) is based upon a manually defined partitioning of the co-array into rings. For optimum results, the azimuthal distribution of station pairs within a single ring should be as uniform as possible in the range of $[0, \pi]$. Considering realistic configurations, there is a trade-off between width of the ring and a good azimuthal coverage within this ring. Within this study we found that uniform azimuthal distribution is by far more important than the width of the ring. Since uniform sampling of azimuths or receiver pairs ij, respectively, assumed in (2) is only achieved for very symmetric configurations, we weight the available autocorrelation functions by $\Delta\varphi_{ij}$. The weights $\Delta\varphi_{ij}$ depend on the azimuthal distribution within each ring. For each ring $\sum \Delta\varphi_{ij} = \pi$ (for details see Bettig *et al.* 2001). We also apply the weighted azimuthal and radial averaging to the normalization factors. For each kth ring with inner and outer radii r_{1_k} and r_{2_k} this results in:

$$\overline{\rho_k}(\omega) = \frac{\frac{1}{\pi} \sum_{ij} \Phi_{ij}(r_{ij}, \varphi_{ij}, \omega) \cdot \Delta\varphi_{ij}}{\frac{1}{\pi} \sum_{ij} \sqrt{\Phi_{ii}(\omega)\Phi_{jj}(\omega)} \cdot \Delta\varphi_{ij}}, \qquad \forall ij, \ r_{1_k} < r_{ij} < r_{2_k}. \tag{10}$$

The accuracy of the averaged autocorrelation coefficients depends on several criteria (Asten 2006). The azimuthal averaging process will be biased due to the finite character of the array or an insufficient distribution of station pairs within a ring (see above). Furthermore, incoherent noise will be present in real data. Finally, the assumptions that the wavefield is stationary and has plane wave character may be violated. The processing here includes three different levels of averaging. At the beginning the autocorrelation at zero lag (coherence) is computed for each station pair and time segment (see eq. 1). Secondly, the autocorrelation coefficients for a particular ring are averaged (see eq. 10). Finally, we calculate mean values and variances (σ_{kl}^2) of the (normal assumed) distribution of all ring-averaged and normalized autocorrelation coefficients $\overline{\rho_k}(\omega)$ for all analysed time segments for a particular ring k and component l. This procedure provides a measure for the uncertainty of the results for further processing in terms of temporal stationarity. For a more advanced uncertainty measure which is not used here (complex part of the averaged autocorrelation), we refer to the recent paper of Asten (2006).

In order to determine the model parameters, we apply a simple grid search. We choose a step width of 0.01 km s^{-1} for velocity (C_R, C_L) and of 0.05 for α. The misfit E between data and model is minimized in a weighted least-squares sense,

$$E(C_R, C_L, \alpha, \omega) = \sqrt{\frac{1}{3 \cdot N} \sum_{k=1}^{N} \sum_{l=1}^{3} \left(\frac{1}{\sigma_{kl}^2}\right) \cdot (d_{kl}(\omega) - g_{kl}(C_R, C_L, \alpha, \omega))^2}, \tag{11}$$

where d_{kl} and g_{kl} denote the measured and the forward calculated averaged autocorrelation coefficient, respectively, and σ_{kl}^2 is the variance estimate.

4 DATA

The studies of Scherbaum *et al.* (2003) and Ohrnberger *et al.* (2004b) (see Section 1) used data of an ambient vibration measurement campaign carried out at the Pulheim site in the LRE within the scope of the SESAME project. In this study we employ the same data set. During the experiment a station array (12 Lennartz LE3D-5s sensors) with an aperture of about 900 m (Fig. 2a) recorded several hours of data during daytime with a sampling rate of 125 Hz.

In order to assess the reliability of 3c-MSPAC analysis, we first start with synthetic data. We simulate ambient vibration wavefields using the receiver array geometry of the field experiment (Fig. 2a). The structure is given by a vertical inhomogeneous model consisting of horizontal layers with constant isotropic velocities. It represents a slightly modified version of the reference model for the LRE (Brüstle & Stange 1999; Brüstle *et al.* 2000) following the inversion of Scherbaum *et al.* (2003) (see model A in Fig. 1 and Table 1). We compute synthetic data sets of different composition and source characteristics using the mode summation algorithm of Herrmann (2001) and a sampling rate of 50 Hz. In order to simulate ambient vibration sources, we use a number of about 4000 point sources (Fig. 2b) with random amplitudes (single force vectors). They are randomly distributed on the surface and in time within a total duration of 10 minutes (Ohrnberger *et al.* 2004b). The sources are restricted to distances of up to 5 km from the centre of the receiver array (Fig. 2b). Additionally, we prepare a second source distribution by removing all sources inside a radius of 1 km ($\approx$200 sources). For this second data set, the curvedness of the wave fronts is therefore significantly reduced. In order to investigate reliability for different wavefield compositions, we simulate successively fundamental-mode Rayleigh waves (vertical-orientated point forces) and fundamental-mode Love waves (horizontal force components). Then, we add their corresponding higher modes as the assumption of only fundamental modes does not have to conform to real observations (see Bonnefoy-Claudet *et al.* 2004, 2005). For both synthetic and real data we choose the same ring configuration from the co-array (six rings, Fig. 2c).

5 RESULTS AND DISCUSSION: SYNTHETIC DATA

5.1 Application of 3c-MSPAC

We average over 29 time segments of frequency-dependent lengths to compute the autocorrelation coefficients, e.g. 80 s at 0.5 Hz and 16 s at 2.5 Hz ($40 * 1/f_c$).

Exemplary, Fig. 3 shows the obtained autocorrelation coefficients of all components and rings for the Rayleigh wave data set together with one standard deviation $\pm\sigma_{kl}$. Stable (Bessel-function-like) autocorrelation curves are obtained. Furthermore, we add the coefficients which correspond to the best-fitting model. A good fit, mainly within the error bounds of the estimated autocorrelation coefficients, can be observed for all rings and components.

Fig. 4 shows the results of the grid searches carried out in the 3-D model space (velocity interval 0–2 km s^{-1}). For plotting reasons the results are shown separately for each model parameter. Each contour plot in Fig. 4 and in the following figures corresponds to a 2-D misfit function $E(m, f_c)$ ($m = C_L, C_R$ or α). For each fixed frequency it takes the misfit values of the minima within 2-D sections perpendicular to the axis of the considered model parameter in the 3-D parameter space. The model parameter with the lowest misfit value m_{Est} (triangles) is plotted together with error bounds. They correspond to $\pm$ one standard deviation according to the definition of the diagonal elements of the model covariance matrix in a least-squares sense (Menke 1989), $\overline{\sigma}_d{}^2(f)|\frac{1}{2}\frac{\partial^2 E(m,f)}{\partial m^2}|_{m=mEst}^{-1}$, where $\overline{\sigma}_d(f)$ is the standard deviation of the data averaged over all rings and components. Furthermore, the dispersion curves used for the simulations are shown in all figures. In order to compare the best-fitting α with theoretical values, we repeat all wavefield simulations for a single station located at the origin of the coordinate system after rotating all source positions onto the east–west axis. Thus, we keep source amplitudes, temporal distribution and distances to the origin of the original sources and obtain Rayleigh and Love waves on separate components. Stacking the transverse (Love waves) and radial (Rayleigh waves) amplitude spectra within each frequency band, we are able to calculate the expected α. Aliasing curves for the velocities are plotted in all figures according to the wavenumber limitation $k_{\min} = 0.0041$ m^{-1} and $k_{\max} = 0.0247$ m^{-1} obtained from the FK array response.

We omit the results for Love waves and the expected α curve in Fig. 4 because of $\alpha = 1$ (only Rayleigh waves). Fig. 4a shows that best-fitting phase velocity and relative fraction of Rayleigh waves are in good agreement with the theoretical fundamental-mode dispersion curve and the theoretical wavefield composition between 0.6 and 2 Hz. Outside that frequency band we observe unstable results and increasing error bars (below 0.6 Hz) or slight aliasing effects (above 2 Hz). This is caused by the resolution limit of the method and the lack of energy in the synthetic data at lower frequencies, respectively (see kink in the autocorrelation curve in Fig. 3 and spectra in Fig. 8).
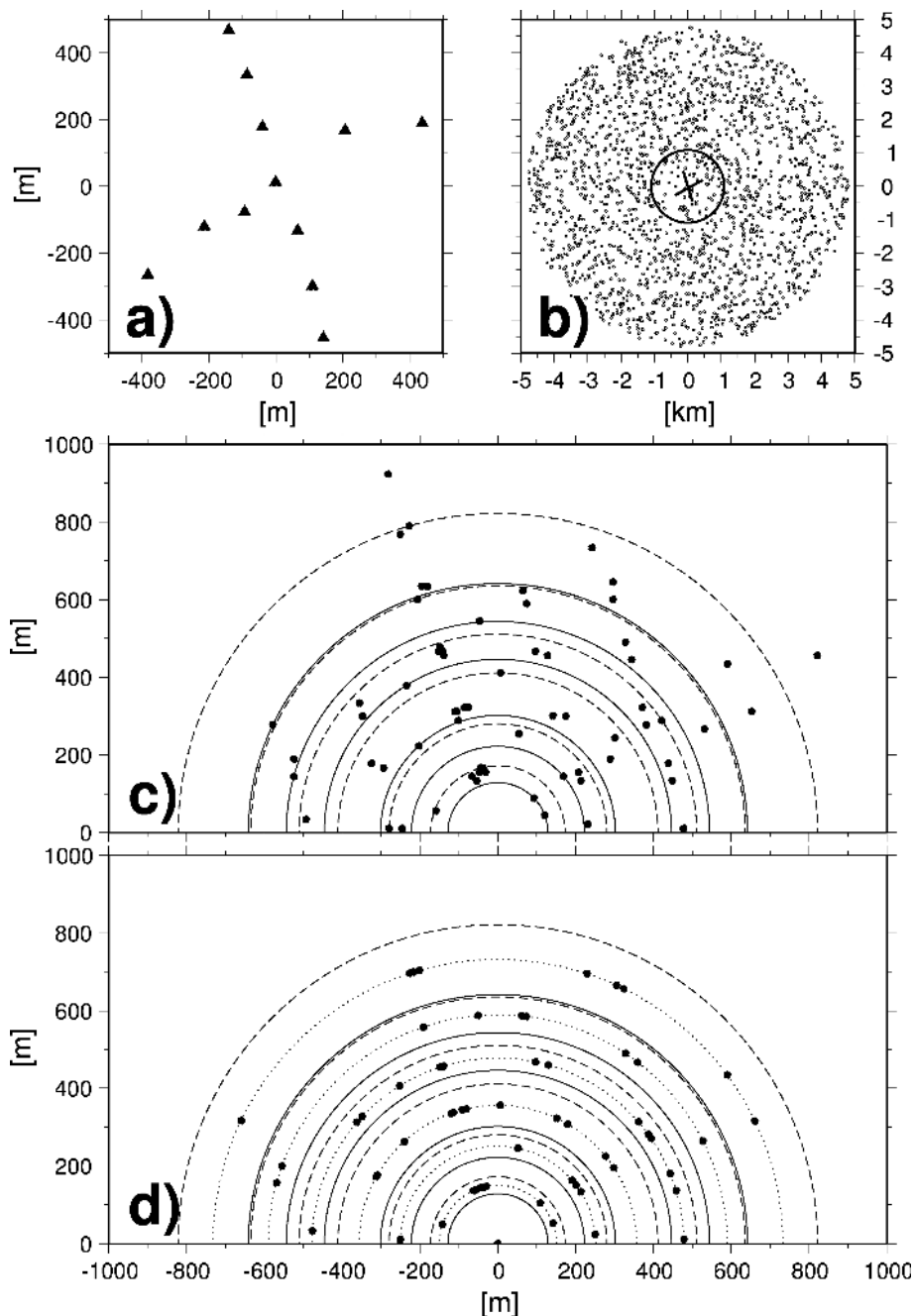
Figure 2. (a) Array configuration of the field experiment in Pulheim. (b) Distribution of point sources on the earth surface used for the ambient vibration simulation (black points). The black circle indicates the area where the sources are omitted in the second simulation in order to avoid excitations inside the array (array shape indicated by crossed lines). (c) Ring configuration for MSPAC analysis (manually selected): Solid semi-circles mark inner ring radii, dashed semi-circles outer ring radii and black points the co-array. (d) Co-array obtained by projecting the station pairs of (c) on the mean ring radius (dotted semi-circles). Use is explained in the text.

If we compare Figs 4(a) and (b), we observe a clear effect of sources close to or inside the receiver array. In contrast to the scenario without close sources (Fig. 4b), the best-fitting α in the previous case (Fig. 4a) vary between 0.75 and 0.95 for frequencies between 1 and 2 Hz. Thus, an apparent fraction of Love waves is falsely implied. Furthermore, the expected theoretical dispersion curves can be determined towards lower frequencies in the absence of close sources. Frequencies in the vicinity of the velocity kink at 1 Hz (see theoretical dispersion curve) are also affected. Deviation from the parallel wave front assumption (SESAME 2005) or undeveloped surface waves at small distances are the most likely causes for these observations.

We proceed with the data set consisting of fundamental Rayleigh and Love waves (Fig. 5a). The best-fitting Rayleigh and Love wave phase velocities are in very good agreement with the corresponding theoretical dispersion curves. Exceptions are the aliasing effects above about 1.5 Hz and around the velocity step near 1 Hz (best values within lower minimum). However, since we additionally plot the error surface

3c spatial autocorrelation technique

Table 1. Pulheim site model A (Brüstle & Stange 1999; Brüstle *et al.* 2000; Scherbaum *et al.* 2003).

Thickness (m)	Vp (m s^{-1})	Vs (m s^{-1})	density (g cm^{-3})
35	542	209	1.762
178	851–1131*	393–522*	1.736–1.85*
80	3085	1619	2.202
80	3525	1850	2.308
80	3913	2054	2.394
80	4265	2238	2.467
80	4588	2408	2.531
80	4888	2566	2.588
80	5170	2714	2.64
49	5387	2828	2.678
Half-space	5916	3416	2.782

*Gradient.
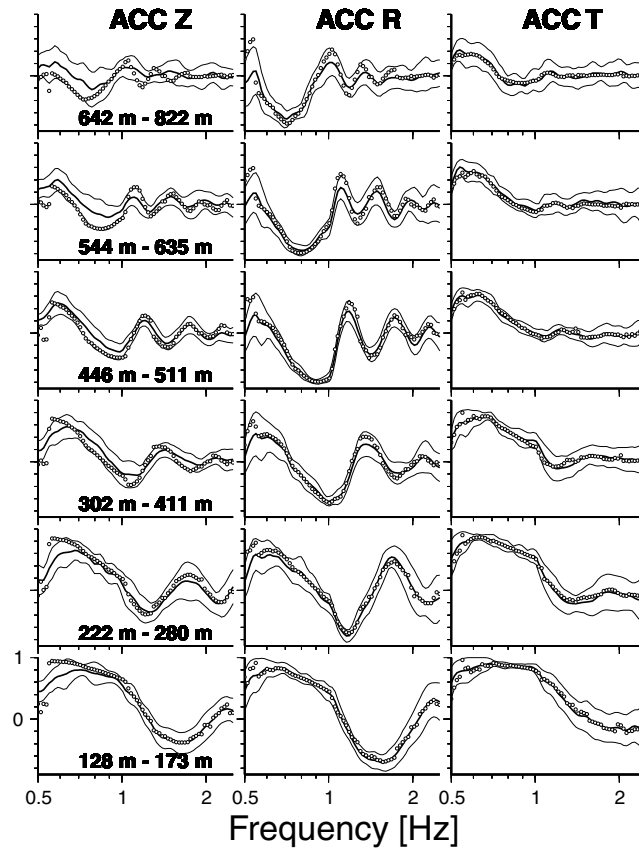
Figure 3. Averaged autocorrelation coefficients (ACC, black solid curves) for each ring and component (vertical: Z, radial R, tangential: T) computed for the synthetic data set containing only Rayleigh waves and ± one standard deviation (thin black solid curves). The inner and outer ring radius for each ring is given in the first figure column (vertical component). The symbols are the autocorrelation coefficients corresponding to the best-fitting model of the grid search.

of the grid search, we are still able to interpret the results correctly by considering the second local minimum. The best-fitting fraction of Rayleigh waves within the stable frequency band varies between 0.25 and 0.45 which is in good agreement with the theoretical curve. Again we also consider the corresponding distant source data set (Fig. 5b). Besides obviously more stable results for lower frequencies and near 1 Hz, we observe that the fraction of Rayleigh waves increases from 40 per cent to about 90 per cent between 1 and 3 Hz confirmed by the theoretical α curve. This observation can be attributed to higher attenuation of Love waves compared to Rayleigh waves at the corresponding frequencies.

In contrast to the azimuthal averaging, the radial distribution of station pairs inside a ring is not taken into account for the radial averaging process (see Theory). It can be argued that this is an inappropriate simplification. Thus, although the width of each ring is considered by MSPAC, traditional SPAC may be preferred. In order to analyse this question further, we simulate a wavefield identical to the data set corresponding to Fig. 5a (close sources), but using a modified receiver array. For this purpose, we simply project all station pairs of the co-array corresponding
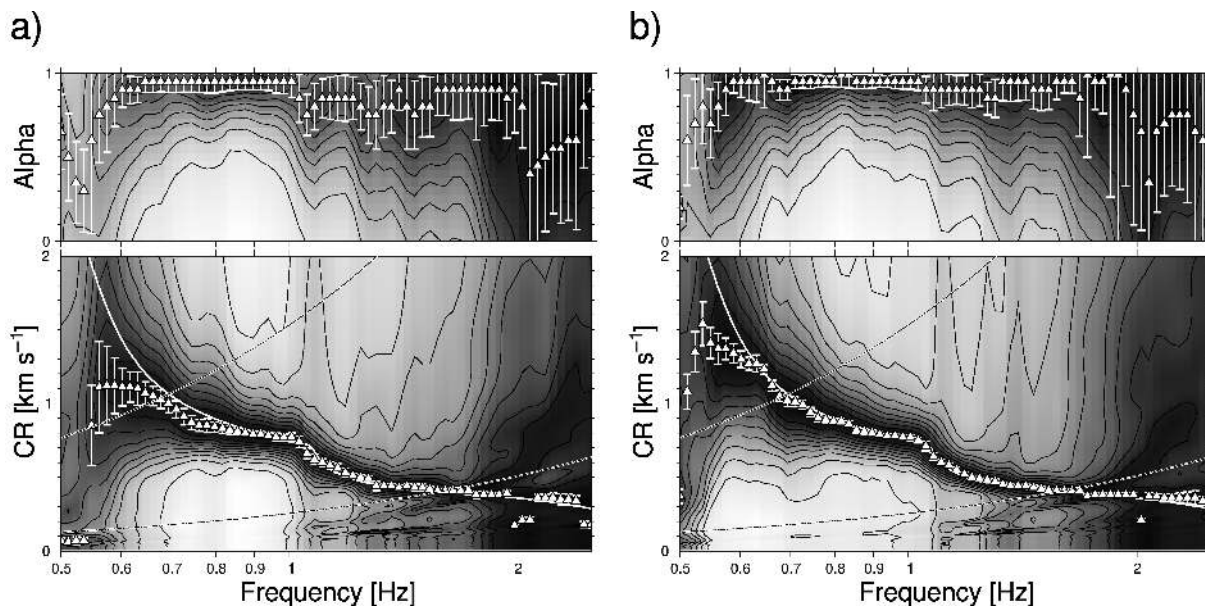
© 2006 The Authors, *GJI*, **168,** 779–796
Journal compilation © 2006 RAS

Downloaded from https://academic.oup.com/gji/article/168/2/779/691582 by U.S. Department of Justice user on 17 August 2022

Figure 4. Contour plots for Rayleigh wave phase velocity (CR) and fraction of Rayleigh waves (Alpha) (here Love wave phase velocity (CL) is omitted) representing the results of the grid search (range corresponds to axis limits). (a) Synthetic data set containing only Rayleigh waves and (b) the same composition but omitting close sources. Black stands for low misfit. Grey scale and contour lines are logarithmic. White triangles are the model parameters corresponding to the lowest misfit and white error bars indicate ± one standard deviation. The white curve shows the theoretical dispersion curve and the thin white (in dark areas)/thin black (in light areas) curves show the aliasing and resolution limitation (see the text).
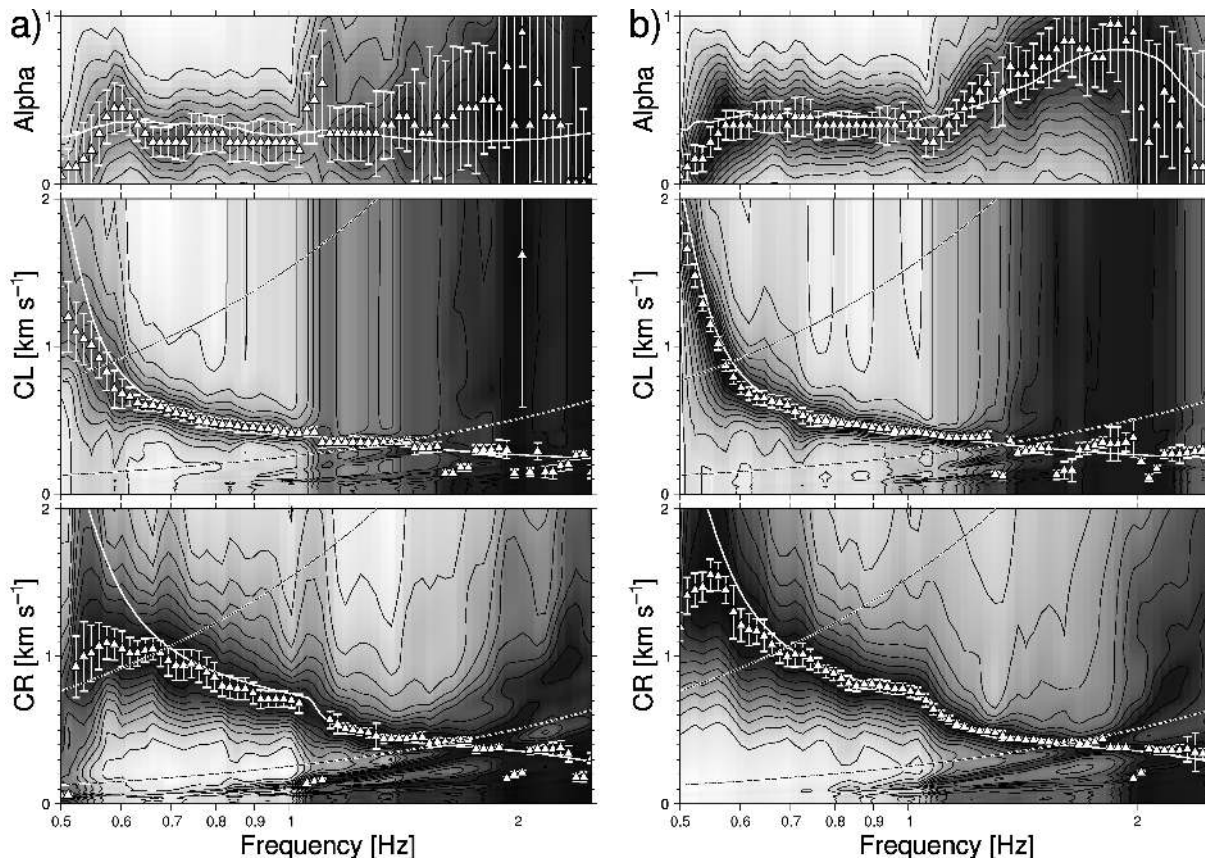

Figure 5. Contour plots for Rayleigh (CR), Love wave phase velocity (CL) and fraction of Rayleigh waves (Alpha) representing the results of the grid search. (a) The synthetic data set containing fundamental-mode Rayleigh and Love waves and (b) the same composition but omitting close sources. The white curve within in upper panel represents the forward-calculated Alpha (for all other symbols and curves see Fig. 4).
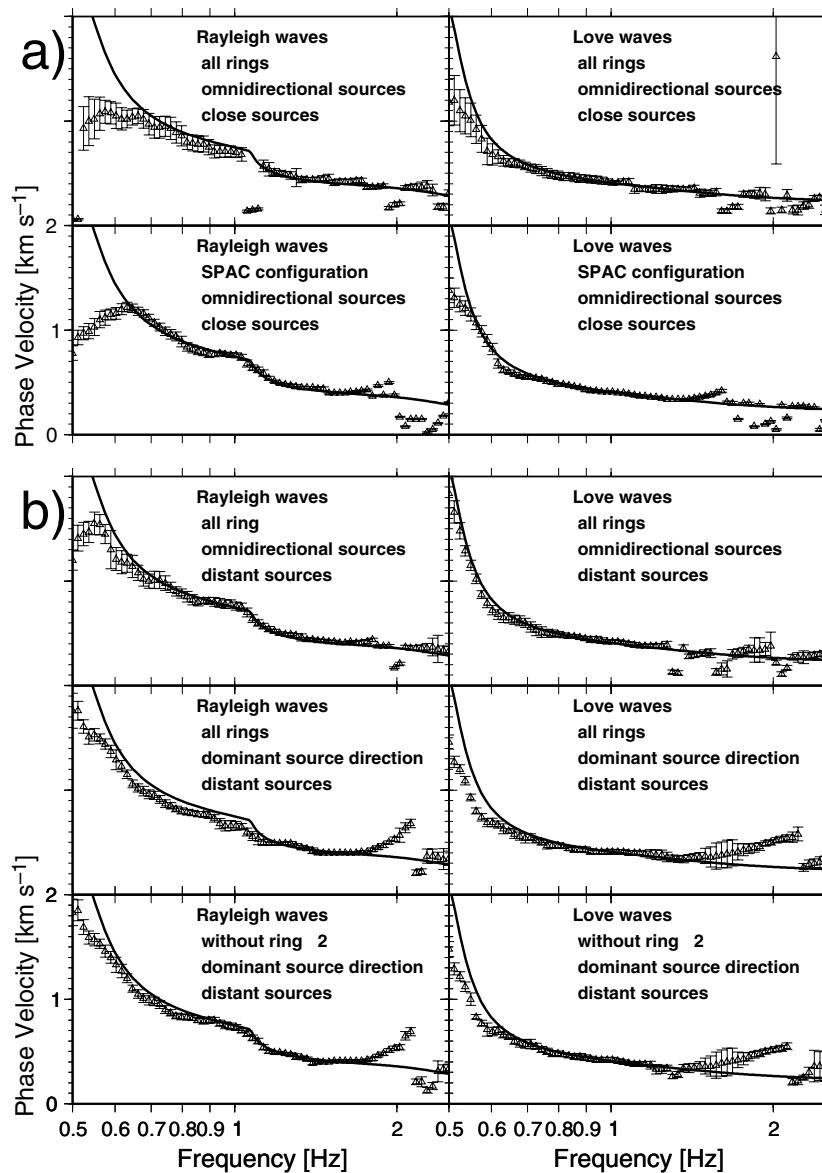
Figure 6. Comparison of theoretical dispersion curves (black curves) and the impact of different source distributions and co-array geometries on the best velocity estimates (triangles with error bars): (a) comparison MSPAC and SPAC (close sources) and (b) impact of source distribution (distant sources).

to the original array layout onto the mean ring radius of the respective ring in radial direction (Fig. 2d). Next, we consider the modified co-array as a new receiver array and compute the wavefield. Since a co-array always contains its corresponding receiver array, we are able to compute and afterwards extract the autocorrelations for the six modified rings. This processing reduces the rings to circles (as required for SPAC) by keeping the azimuthal distribution of the original co-array. The formulae for SPAC (4,5 and 6) are used to calculate the grid search misfit. By comparison of the obtained velocities (Fig. 6a), we find smaller error bars and less aliasing effects for the modified co-array. However, we find the differences for the phase velocity values negligible and conclude that the radial averaging does not distort the results. Considering the arguments in favour of arbitrary array configurations given above, disadvantages of MSPAC can be neglected.

The finite character of the co-array affects the quality of the results, particularly for a unidirectional distribution of ambient vibration sources. In order to test the goodness of our co-array geometry and ring configuration, we process a data set employing a modified source distribution. We place 1260 sources (background) between radii of 1 and 5 km and, representing the dominant azimuth range, 1760 sources inside a circle of 1 km radius centred at a location 1.5 km westward and 2.5 km southward from the array midpoint. Since we observe clear deviations from the expected dispersion curves for the estimated velocities (Fig. 6b), we have to look at the distribution of station pairs in more detail. As already reported by Ohrnberger *et al.* (2004b) the second ring (starting from the smallest one) has got a strong unidirectional distribution of station pair compared to the other rings (see Fig. 2). Excluding this ring from the grid search process, the results are in a clearly better accordance with the omnidirectional source distribution (Fig. 6b).
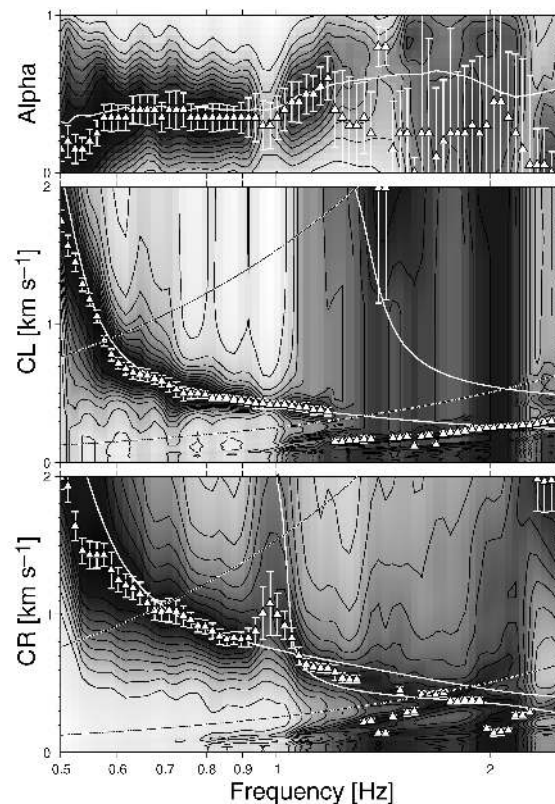
Figure 7. Contour plots for Rayleigh (CR), Love wave phase velocity (CL) and fraction of Rayleigh waves (Alpha) representing the results of the grid search for the synthetic data set containing both fundamental and higher mode surface waves (unmodified array, distant source scenario), (symbols and curves see Figs 4 and 5).

In the conventional implementation SPAC and MSPAC are confined to resolve one single mode of Rayleigh and Love waves. Nevertheless, we process a data set containing higher modes (Fig. 7, distant omnidirectional sources). This approach allows us to investigate the bias of the velocity estimates in the presence of several modes and to decide whether dominant higher modes can be identified. This is crucial for the analysis of real data of unknown composition. The results show clear effects of higher modes (compare Figs 5b and 7). Up to 0.9 Hz the Rayleigh wave velocities still fit the theoretical fundamental mode. However, between 0.9 and 1 Hz a clear onset of the first higher mode can be observed followed by values in between both modes. For higher frequencies we have to interpret the whole error surface since significant aliasing effects affect the best model parameters. Again, a clear low misfit area in between both theoretical mode branches can be observed. Due to the inability of multiple-mode resolution, this observation corresponds to an effective phase velocity. The fundamental mode seems to dominate for frequencies above 1.5 Hz because the difference between best-fitting velocities (which are not affected by aliasing) and theoretical fundamental-mode velocities is very small. We do not observe any evidences for higher mode Love waves. However, due to the aliasing effects above 1 Hz, we cannot give a clear interpretation. Both, the forward computed and the estimated fractions of Rayleigh waves do not seem to change significantly compared to the fundamental-mode data set.

Fig. 8 shows phase velocities computed by FK analysis for all three components (Z,N,E) and the Rayleigh- and Love wave velocities obtained by MSPAC for two data sets (close source case). In particular we use the CVFK method (after Kvaerna & Ringdahl 1986) based upon a sliding time window analysis and a grid search in the wavenumber plane (resolution: 10 degrees and 0.025 km s^{-1}). As expected for the Rayleigh wave data set, the median CVFK velocities of all components do not differ and, furthermore, are in good agreement with the 3c-MSPAC Rayleigh wave velocities (Fig. 8a). Both lower and upper frequency limits, which correspond to resolution and aliasing limitations, appear to be similar for both methods. Considering the kink in the dispersion curve at 1 Hz, the vertical CVFK velocities do not sample the dispersion curve correctly compared to MSPAC. We made similar observations for the data set that contains Rayleigh and Love wave fundamental modes (Fig. 8b). The most striking feature here is that the horizontal CVFK velocities show a mixture of both Rayleigh and Love wave velocities. For an equal contribution of both types of waves, we would expect velocities corresponding to the mean of theoretical Rayleigh and Love wave velocity (Tokimatsu 1997). Thus, evaluation of the horizontal CVFK velocities implies a value for α less than 0.5. This is an independent confirmation of the values found by 3c-MSPAC analysis and by forward computation.

5.2 Inversion of dispersion curves

In order to investigate the reliability of Love waves for shear wave velocity (*Vs*) inversion, we carry out inversions of Rayleigh and Love wave dispersion curves (both separately and simultaneously). As inversion method, we use the neighbourhood algorithm of Sambridge (1999a,b)
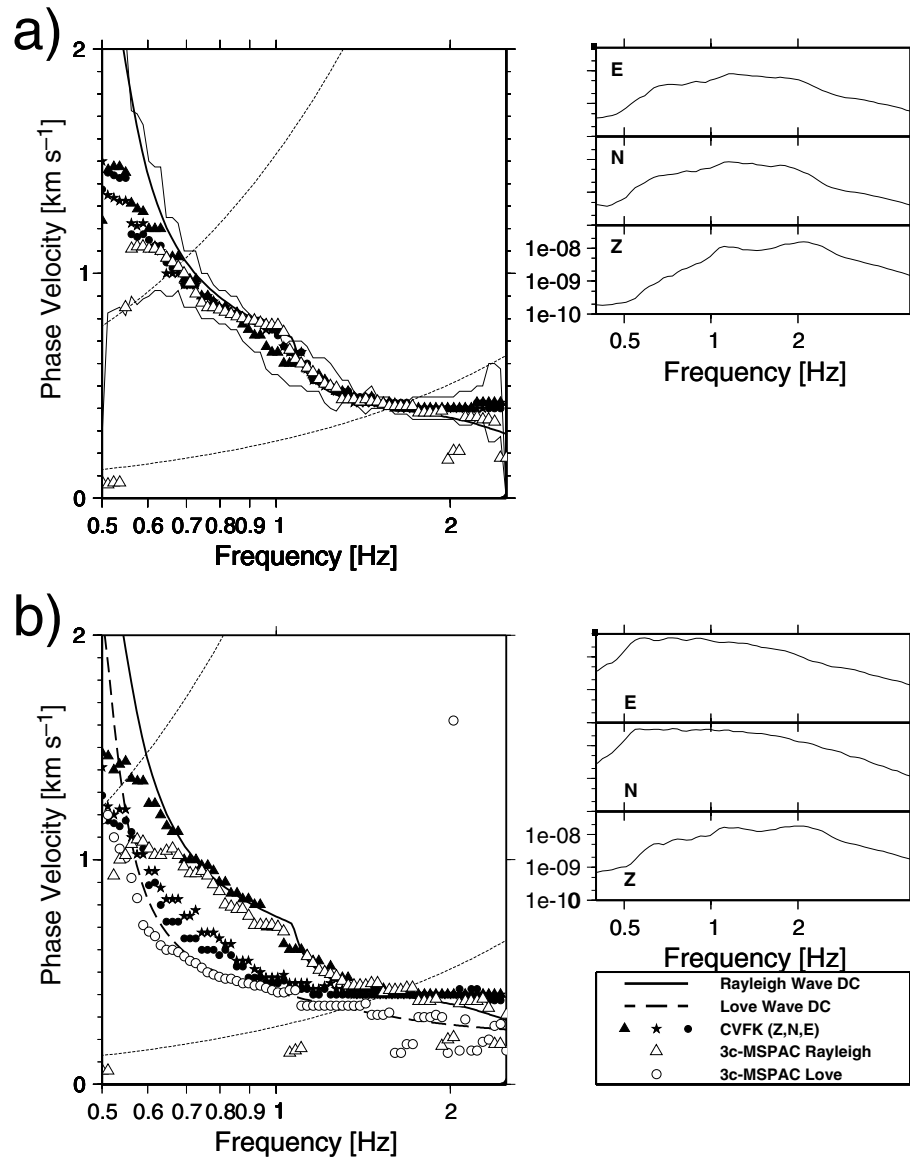
Figure 8. Median CVFK velocities (black symbols) with ± median deviation (thin solid black curves) for all three components compared to the best 3c-MSPAC and theoretical Rayleigh and Love wave velocities (white symbols and black curves). The thin black dashed curves are the aliasing curves. (a) Synthetic data set (close source case) containing only Rayleigh waves. (b) Synthetic data set (also close source case) containing fundamental-mode Rayleigh and Love waves. We omit the median deviation for the horizontal components in (a) and completely in (b) for clarity. They are comparable with vertical CVFK in (a). Additionally, the amplitude spectra (log–log) of all data sets are shown (top right in a and b, same scale for all).

successfully employed within the SESAME project (Wathelet *et al.* 2005). The aliasing corrected (second minimum) Rayleigh (0.55–2.5 Hz) and Love wave velocities (0.5–2.3 Hz) of the fundamental-mode data set are used (see Fig. 5b). Furthermore, we also employ the estimated dispersion curves of the higher mode data set (Rayleigh: 0.58–1.4 Hz, Love: 0.5–1.24 Hz, see Fig. 7).

For parametrization of the model space we choose two layers over half-space. Due to the limited depth resolution which results from the limited frequency band, a finer parametrization in order to obtain the velocity structure below the dominant seismic contrast would make no sense. Note, that there is a general trade-off in the model parameter space between thickness and *Vs* of a layer (positive correlation) since the theoretical model is characterized by increasing averaged velocities with depth. Furthermore, considering all generated models, generally there is a higher resolution in terms of velocity compared to depth.

Figs 9(a)–(c) show the inverted models for the fundamental-mode data set. There is a good agreement between best models of separate Rayleigh wave inversion (a), Love wave inversion (b), and theoretical shear wave velocity profile. Joint inversion yields a best model that does not fit the depth of the dominant velocity contrast (Fig. 9c). Considering the whole set of good model fits, we see a better resolution of the interface depth compared to the separate inversion runs. The results for the data set containing higher modes are shown in Figs 9(d)–(f), respectively. In spite of a narrower frequency band (0.5–1.24 Hz) compared to the previous case, the Love wave inversion correctly yields the theoretical *Vs* profile because no effects of higher modes could be observed in the dispersion curve (see above). In contrast, the Rayleigh
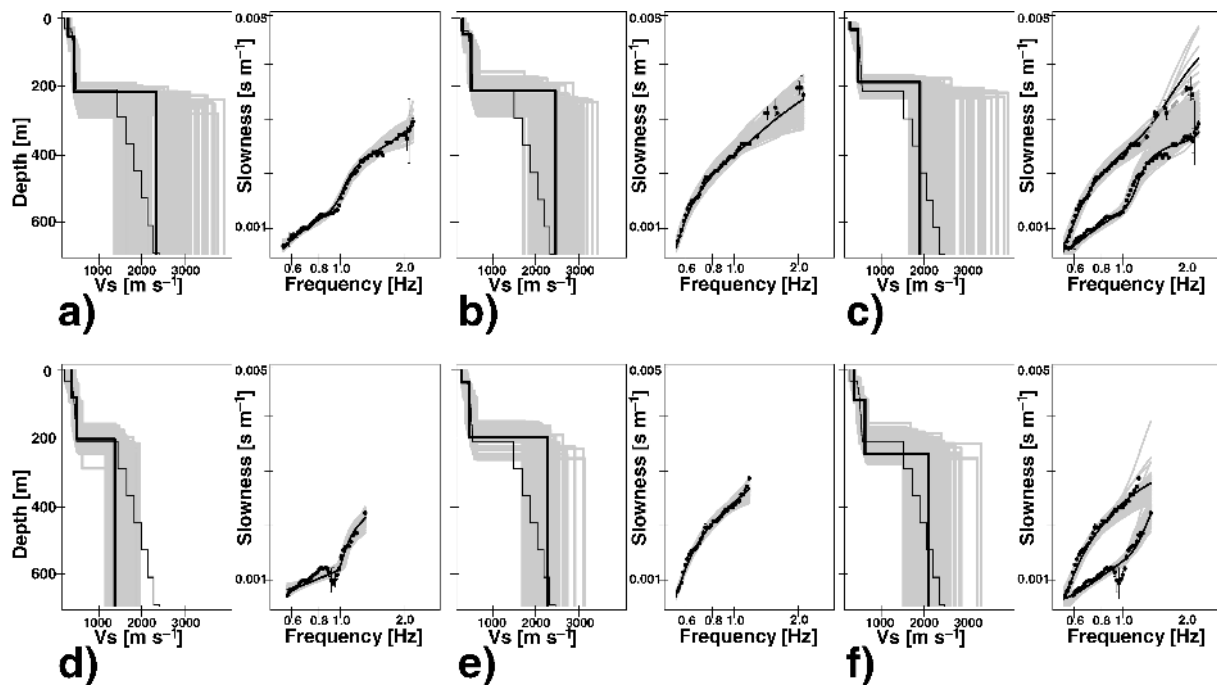
Figure 9. Inversion of *Vs* profiles (synthetic data). The grey areas display the set of good model fits (*Vs*-profiles and dispersion curves). The thick black curves/lines stand for the best-fitting model. The black circles correspond to the dispersion curve employed for inversion (slowness vs. frequency). The thin black *Vs* profile indicates the theoretical model used for the wavefield simulation. (a) Rayleigh wave, fundamental-mode data. (b) Love wave, fundamental-mode data. (c) Joint inversion, fundamental-mode data. (d) Rayleigh wave, higher mode data. (e) Love wave, higher mode data. (f) Joint inversion, higher mode data.

wave dispersion curve is clearly affected by higher modes. Thus, as expected, the separate and also the joint inversion result in biased models. In particular the average half-space velocity is underestimated (Fig. 9d) and a misfit of the upper (Fig. 9d) or lower (Fig. 9f) velocity contrast can be observed.

6 RESULTS AND DISCUSSION: REAL DATA

6.1 Application of 3c-MSPAC

For the processing of the data recorded at the Pulheim site, we use the same parameters and frequency bands as for the synthetic data. However, due to the availability of longer records we choose a longer time window of 20 min chosen visually from the record (63 averaged segments, individual lengths unchanged). Furthermore, a broader grid search interval for velocity turned out to be more appropriate (0–2.5 km s^{-1}).

Fig. 10(a) presents the computed and fitted averaged autocorrelation coefficients. We derive a Rayleigh wave dispersion curve by taking directly the best-fitting phase velocities in a frequency band between 0.54 and 1.3 Hz (Fig. 10b). The frequency range is even broader (higher frequencies) for the best Love waves dispersion curve. However, reliable Rayleigh wave velocities outside the frequency band regarded above can be derived following the misfit minimum in the velocity–frequency grid towards higher frequencies. Here, the absolute minimum at lower velocities can be identified as an aliasing effect.

Within the stable frequency band up to 1.3 Hz we observe a low fraction of Rayleigh waves between 10 per cent and 35 per cent. This implies a dominance of Love waves in the horizontal ambient vibration wavefield at the Pulheim site. In order to obtain the model parameters located within the second misfit minimum, we restrict the grid search interval from 0.3 to 2.5 km s^{-1}. The new best-fitting model is shown in Fig. 11. The apparently higher fraction of Rayleigh waves between 1.3 and 2 Hz turn out having been an aliasing effect (compare Figs 10b and 11a). The corrected values stay at about 30 per cent and, thus, seem to be more or less on the same level over the whole analysed frequency band.

Between 0.5 and 0.6 Hz both α and the best Rayleigh wave dispersion curve show a characteristic trough. An explanation may be lack of energy on the vertical component (maximum of the Rayleigh wave ellipticity) and a energy maximum on the horizontal components (Airy phase of Love waves), respectively (see Fig. 11b). For comparison, direct estimation of the fundamental frequency at this site from H/V spectral ratios yielded 0.5 Hz (Scherbaum *et al.* 2003), 0.5–0.55 Hz (Ohrnberger *et al.* 2004a) and 0.54 Hz (Parolai *et al.* 2005).

Fig. 11b summarizes the results for the best-fitting Rayleigh and Love wave velocities and the results of 3c-CVFK analysis of the same time window. There is a good agreement between vertical CVFK and the 3c-MSPAC Rayleigh wave velocities above 0.8 Hz. Due to the dominance of Love waves (90 per cent), also horizontal CVFK velocities fit the estimated MSPAC Love wave dispersion curve. However, the difference between CVFK and MSPAC results increases at lower frequencies. This can be related to the decreasing resolution capability of
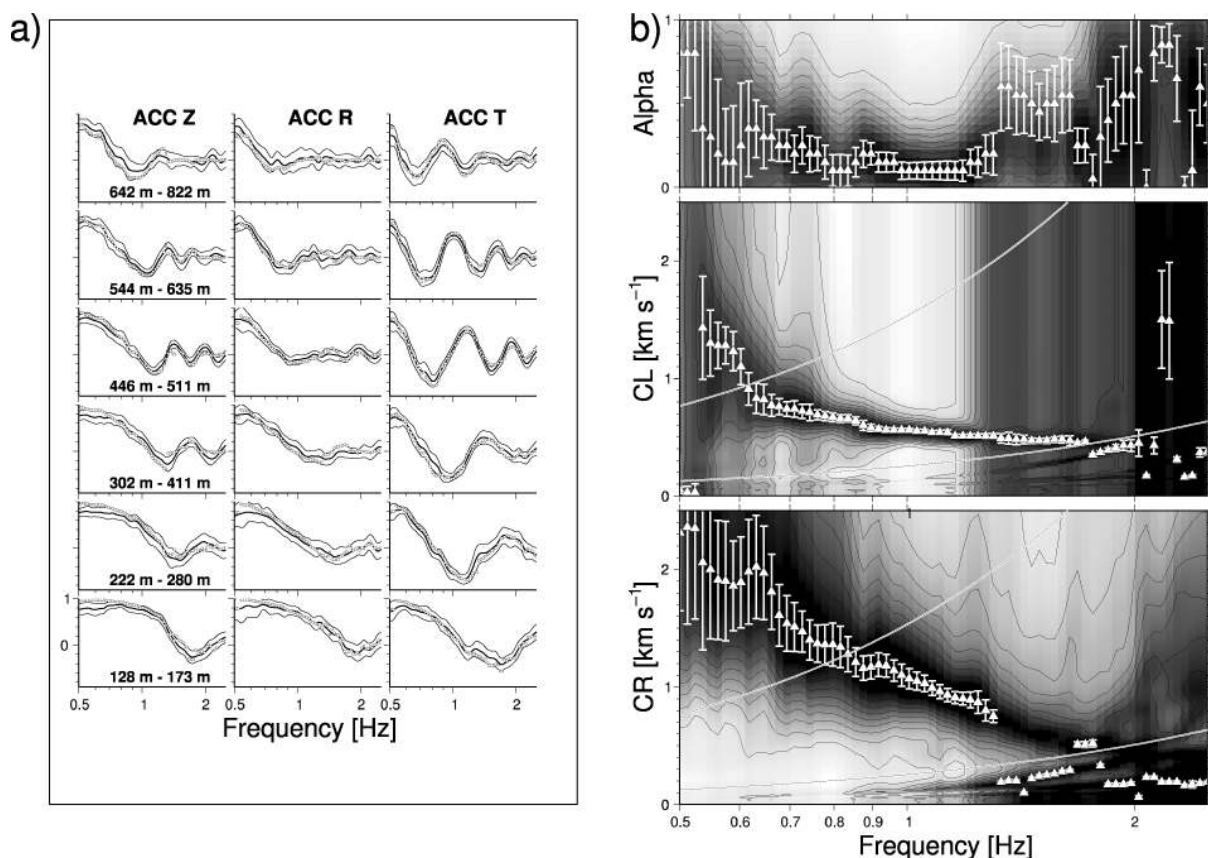
Figure 10. (a) Averaged autocorrelation coefficients (black solid curves) for each ring and component (vertical: Z, radial R, tangential: T) computed for the data recorded at the Pulheim site and ± one standard deviation (thin black solid curves). The inner and outer ring radius for each ring is given in the first figure column (vertical component). The symbols are the autocorrelation coefficients corresponding to the best-fitting model of the grid search. (b) Contour plots for Rayleigh (CR), Love wave phase velocity (CL) and fraction of Rayleigh waves (Alpha) representing the results of the grid search for the real data set (for symbols and curves see Fig. 4).

the methods and the lack of energy on the vertical component (H/V peak). Moreover, the increasing α may explain the difference between Love wave velocities and horizontal CVFK.

In order to evaluate and discuss the different velocity–depth profiles that are existing for the Pulheim site (see Fig. 1), we compare our results with the corresponding forward computed dispersion curves (Fig. 11c). Starting with the slightly modified reference model for the LRE (model A), which was used to compute the synthetic data sets, we observe that Rayleigh and Love dispersion curves are consistently shifted to higher velocities compared to the theoretical fundamental mode curves. However, they show a similar trend over frequency.

The deviation between local site and regional reference model was also reported by Ohrnberger *et al.* (2004b) and Scherbaum *et al.* (2003) who made use of the same data set. In both studies modified velocity depth profiles were derived using different approaches and parametrizations. Scherbaum *et al.* (2003) (model B, see Fig. 1 and Table 2) only inverted for the depth of the dominant seismic contrast, the shear wave velocity at the surface and the velocity exponent of the assumed power-law behaviour of the velocities over half-space (Budny 1984). The power-law depth function for *Vp* had been fixed. Ohrnberger *et al.* (2004b) also enabled the *Vp* profile and the half-space velocity to be free parameters. Furthermore, these authors used the neighbourhood inversion algorithm of Sambridge (1999a,b) which provides an advanced characterization of the model space. In contrast Scherbaum *et al.* (2003) employed joint inversion of Rayleigh wave ellipticities and dispersions curve (0.7–2.2 Hz). A similar approach was used by Parolai *et al.* (2005) and Picozzi *et al.* (2005) (model D, see Fig. 1 and Table 2). Considering the best models inverted from the Rayleigh wave dispersion curve, Ohrnberger *et al.* (2004b) concluded that the data can be explained by model B after slightly modifying the *P* wave velocities. Fig. 11(c) shows that the Rayleigh wave dispersion curve of model B and the velocities obtained from 3c-MSPAC and CVFK fit well for frequencies higher than 0.65 Hz. Model D shows slightly lower velocities above 0.75 Hz. However, it fits the MSPAC results better than model B below. Due to the lack of energy (MSPAC) and decreasing resolution (CVFK), MSPAC and CVFK do not match with model B and D at lower frequencies. Furthermore, the Love wave dispersion curves of model B and D fit our results over a broad frequency range. However, for frequencies below 0.75 Hz model B shows strong deviations.

By means of a borehole station at 350 m depth and a strong motion station at the earth surface, Ohrnberger *et al.* (2004a) independently tested model B. SH transfer functions were computed from local earthquake recordings and simulated events based on model B. In order to explain the mismatch between observed and forward computed transfer functions and a time delay found for the SH waves between borehole
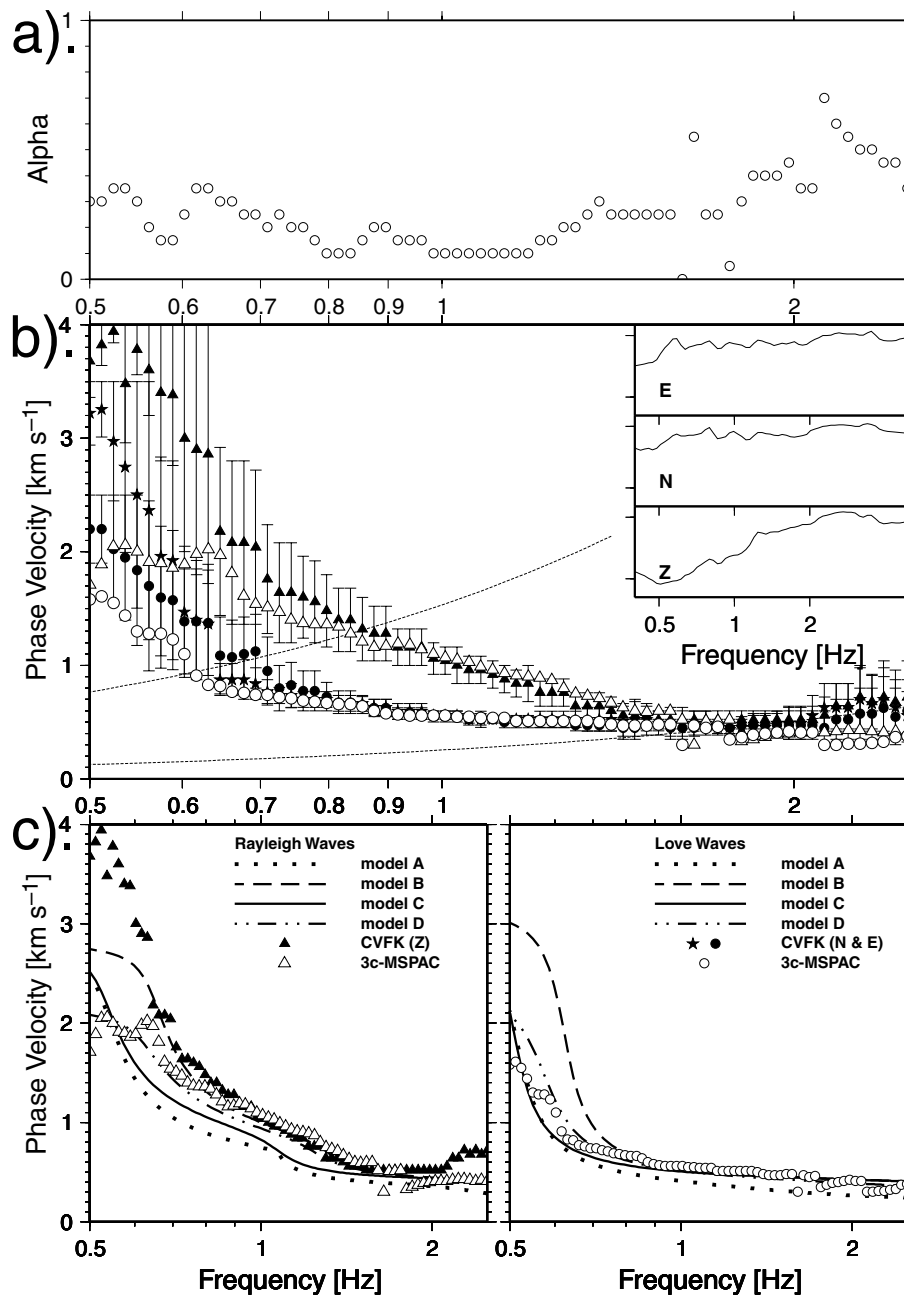
Figure 11. (a) Best-fitting fraction of Rayleigh waves corresponding to the MSPAC velocities in 11b. (b) Median CVFK values (black symbols) with standard deviation (error bars) for the vertical, north and east component compared to the aliasing corrected (restricted grid search) best MSPAC Rayleigh and Love wave velocities (white symbols) for the data set measured at the Pulheim site (legend see 11c). The thin black dashed curves represent the aliasing curves. Additionally, the amplitude spectra of all the data are shown (top right, log–log). (c) Comparison of estimated Rayleigh and Love wave velocities with forward calculated dispersion curves. See the text for details.

and surface station, the depth of the seismic contrast of model B was increased by 50 m (model C, see Fig. 1 and Table 2). In that way the underestimation of the sediment thickness was corrected. Fig. 11c displays the fundamental-mode dispersion curves corresponding to model C. In contrast to model B, the Love wave dispersion curve fits the 3c-MSPAC Love wave velocities over nearly the whole frequency band. Below 0.65 Hz the MSPAC velocities are located between the dispersion curves of model C and D. On the other hand we observe consistently lower Rayleigh wave velocities for model C.

6.2 Inversion of dispersion curves

Since the Pulheim site models (B, C and D) were obtained independently employing different methods or approaches, we do not have a best model that is closest to geological reality. As discussed, each model is able to explain parts of our results. The deeper velocities contrast of

Table 2. Pulheim site model B (Scherbaum *et al.* 2003), C (Ohrnberger *et al.* 2004a) and D (Parolai *et al.* 2005; Picozzi *et al.* 2005).

	Models B and C				Model D		
Thickness (m)	Vp (m s^{-1})	Vs (m s^{-1})	Density (g/cm^3)	Thickness (m)	Vp (m s^{-1})	Vs (m s^{-1})	Density (g/cm^{-3})
10	701	270	1.7	5	701*	125	1.7*
10	1676	332	2.1	13	1900*	319	2.1*
20	1784	396	2.1	15	1980*	302	2.1*
20	1837	430	2.1	33	1980*	433	2.1*
20	1873	454	2.1	23	1980*	476	2.1*
20	1900	473	2.1	23	1980*	434	2.1*
20	1922	488	2.1	116	1980*	577	2.1*
20	1940	501	2.1	Half-space	5000*	2392	2.7*
20	1956	513	2.1	*Used for forward computation, but not taken from			
20	1970	523	2.1	cited study (values are based on model B).			
15(B) 65(C)	1981	531	2.1				
Half-space	5500	3160.9	2.7				

model C claimed by Ohrnberger *et al.* (2004a) explains the obtained Love wave dispersion curve, whereas the original depth given by model B seems to match with propagation of Rayleigh waves. Thus, fixing the depth structure and the shear wave profile of Ohrnberger *et al.* (2004a), as the Love wave velocity only depend on these parameters, we have to modify the Vp velocities in order to fit the observed Rayleigh wave dispersion curve. However, this would require a large increase of Vp to values above about 6 km s^{-1} (what is obviously not realistic) because the effect of Vp on the Rayleigh wave velocity is small compared to Vs.

Consequently, we invert the measured Rayleigh and Love wave dispersion curves for a new 1-D velocity–depth profile in order to compare the results with the available site models. Again we use both dispersion curves simultaneously and separately. The model space is parametrized by two layers over half-space with a power-law behaviour for the velocity–depth structure in the second layer. Fig. 12 shows the results of the inversions and the Vs-profiles of model B, C and D. The inverted models confirm the velocity structure above the dominant velocity contrast for all site models. Furthermore, we obtain models for separate inversion (12a: Rayleigh 0.65–1.5 Hz, 12b: Love 0.5–1.5 Hz) consistent in depth with the dominant seismic contrast of models C and D. Simultaneous inversion of Rayleigh and Love wave dispersion curves (Fig. 12c) results in models fitting the dispersion curves less satisfyingly. However, in terms of resolution (see family of best models) results are comparable with the separate inversion approach. Considering the results of the inversion, we finally propose a shear wave velocity model for the Pulheim site with an interface depth between 220 and 270 m and a half-space velocity between 2000 and 2750 m s^{-1}. That uncertainty range includes the interface depths of model C and D, but clearly reduces the half-space velocity compared to model B and C.
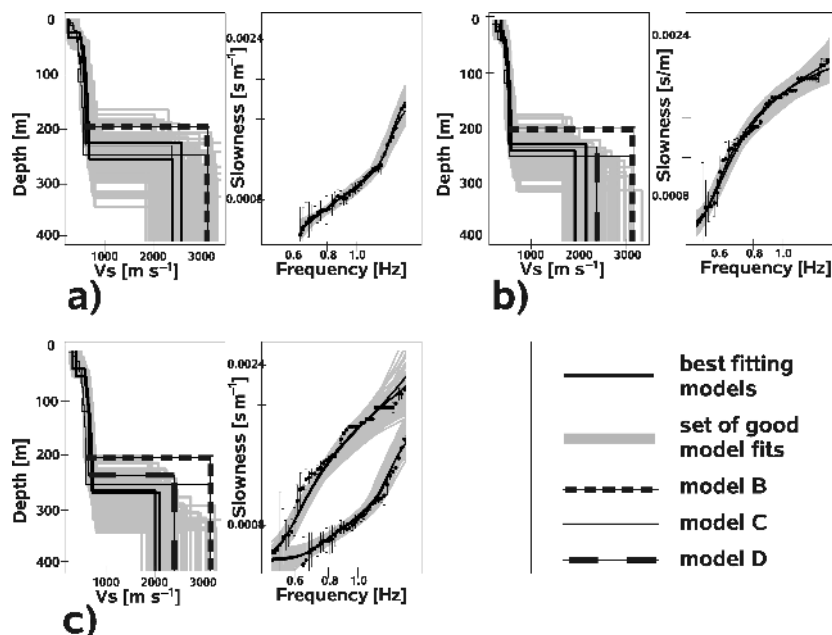

Figure 12. Inversion of Vs profiles (real data). The grey areas display the set of good model fits (Vs-profiles and dispersion curves). The thick black lines/curves stand for the two best models. The black circles correspond to the dispersion curve employed for inversion (slowness vs. frequency). The other Vs profiles indicate the existing site models for Pulheim (model B, C, D, see legend). (a) Rayleigh wave (b) Love wave (c) joint inversion.

Higher modes of surface waves can be present in ambient vibrations as shown e.g. by Tokimatsu (1997). The analysis of synthetic data has shown that increasing phase velocities with frequency followed by an decreasing effective phase velocities can be an evidence for a higher mode onset (see above). Here, we do not observe such a feature or any other evidences for dominant higher modes. On the other hand we cannot rule out some small contribution of higher modes at higher frequencies. However, there is a broader separation of the theoretical fundamental and first higher mode Love dispersion curve (Fig. 7) which should lead to an easily detectable effect of a higher mode onset on the measured dispersion curve. The analysis of synthetic data did not show such an effect for Love waves. Therefore, through the comparison of the real data inversion results using either Rayleigh or Love waves, we obtained support for the assumption of lack of higher modes in the data because the models do not differ significantly.

7 CONCLUSIONS

In this paper, we describe the extension of the modified spatial autocorrelation method (MSPAC) on three-component array analysis and its application to seismic ambient vibrations. We show that the determination of both Rayleigh and Love wave fundamental-mode dispersion curves and their respective portion works very well and reliably for both synthetic and measured data. Therefore, it is on an equal footing with conventional methods like vertical CVFK and vertical SPAC for estimation of Rayleigh wave dispersion curves. Moreover, the use of all three spatial components of ambient vibrations yields reliable results for the relative fraction of Rayleigh and Love waves and the Love wave dispersion curves.

We can show with synthetic data that the 3c-MSPAC method is well suited to determine the phase velocities and the fraction of Rayleigh waves within a frequency band compatible to the array size. Compared to Rayleigh waves, the Love wave dispersion can be observed towards lower frequencies. Furthermore, ring selection from the co-array is preferably done with thin to moderate ring widths so that an omnidirectional distribution of station pairs within each ring is ensured. The absence of sources close to or inside the array improves dispersion curve estimates.

For synthetic data Love waves dominate on the horizontal components (>50 per cent) except at higher frequencies for distant sources. The frequency dependence is possibly an effect of different attenuation for Love and Rayleigh waves, whose dependence on the Vs structure is an aspect of future studies.

Inversion of Love wave dispersion curves for the 1-D velocity–depth profile confirms the results of the commonly preferred Rayleigh wave inversion. Moreover, starting with Love wave inversion is preferable in the presence of higher modes due to the broader mode separation of Love waves. Forward computation of fundamental and higher mode Rayleigh wave dispersion curves then allows for identifying correctly the dispersion curve branches of Rayleigh waves. This is crucial for using advanced inversion scheme that include fundamental and higher modes.

We observe differences between apparent velocities obtained from vertical CVFK and Rayleigh wave dispersion curves derived by MSPAC at the lower and upper frequency limit for real data recorded at the Pulheim site (LRE, Germany). While CVFK seems to be less affected by aliasing at higher frequencies, MSPAC is able to resolve the dispersion curves and the fraction of Rayleigh waves at lower frequencies. For synthetic data no significant differences are found. In any case we recommend to use 3c-MSPAC and CVFK together in future studies as they complement one another.

Supported by studies at other sites in the past, we observe a preponderance of Love waves (65-90 per cent) on the horizontal components of ambient vibrations. Generally, this preponderance benefits the determination of Love wave dispersion curve. Moreover, this fact should be considered in the context of Rayleigh wave ellipticity inversion based upon H/V spectral ratios. Here, often the proportion of Love waves is neglected or assumed to have an empirical value (e.g. 50 per cent). We do not observe perceivable effects of higher modes in this data set. However, synthetic tests show that an identification may be possible in the case they are present. The determination of the Love wave dispersion curve allows to evaluate existing subsurface models derived by different approaches at the Pulheim site. The results of the inversion for 1-D velocity–depth profiles using separately Rayleigh and Love wave dispersion curves show a consistency with models derived by Ohrnberger *et al.* (2004a) and Parolai *et al.* (2005).

REFERENCES

Aki, K., 1957. Space and time spectra of stationary stochastic waves, with special reference to microtremors, *Bull. Earthquake Res. Inst. Tokyo Univ.,* **35,** 415–457.

Arai, H. & Tokimatsu, K., 2000. Effects of Rayleigh and Love waves on microtremor H/V spectra, *Proceeding of the 12th World Conference on Earthquake Engineering 2000,* **paper No. 2232/4/A**.

Asten, M.W., 1976. The use of microseisms in geophysical exploration, *PhD thesis*, Macquarie University.

Asten, M.W. & Henstridge, J.D., 1984. Array estimators and the use of microseisms for reconnaissance of sedimentary basins, *Geophysics,* **49**(11), 1828–1837.

Asten, M.W., 2006. On bias and noise in passive seismic data from finite circular array data processed using SPAC methods, *Geophysics,* **71**(6), 153–162.

Bard, P.Y., 1998. Microtremor measurements: A tool for site effect estimation?, in *State-of-art-paper, Second Int. Symposium on the Effects of Surface Geology on Seismic Motion,* Vol. 3, pp. 1251–1279, eds Irikura, K., Kudo, K., Okada, H. & Sasatani, T.

Bard, P.Y., 2004. The SESAME project: an overview and main results, *13th World Conference on Earthquake Engineering, Vancouver, August 2004,* **paper No. 2207**.

Bettig, B., Bard, P.Y., Scherbaum, F., Riepl, J., Cotton, F., Cornou, C. & Hatzfeld, D., 2001. Analysis of dense array noise measurements using the modified spatial auto-correlation method (SPAC): application to the Grenoble area, *Bollettino di Geofisica Teorica ed Applicata,* **42**(3/4), 281–304.

Bonnefoy-Claudet, S., Bard, P.Y. & Cotton, F., 2004. Final report, WP08—Nature of noise wavefield, *SESAME-Project, EVG1-CT-2000-00026,* **Report-Nr.: D13.08**, http://sesame-fp5.obs.ujf-grenoble.fr.

Bonnefoy-Claudet, S., Cotton, F. & Bard, P.Y., 2005. The nature of the seismic noise wavefield: implications for site effects studies, *Earth Science Review,* in press.

Brüstle, W. & Stange, S., 1999. Geologische Untergrundklassen zum Entwurf von Normspektren für DIN4149 (neu), *LGRB Baden-Würtemberg,* **AZ: 3480.01/98-4764**.

Brüstle, W., Geyer, M. & Schmückling, B., 2000. Karte der geologischen Untergrundklassen für DIN4149(neu), Abschlussbericht, *Fraunhofer IRB Verlag, Stuttgart,* **Best.Nr. T2926, ISBN 3-8167-5766-9**, 60 pp.

Budny, M., 1984. Seismische Bestimmung der bodendynamischen Kennwerte von oberflaechennahen Schichten in Erdbebengebieten der Niederrheinischen Bucht und ihre ingenieurseismologische Anwendung, *PhD thesis* (in German), Geologisches Institut der Universität zu Köln, **Special publication No. 57**, 209 pp.

Cháves-García, F.J., Rodriguez, M. & Stephenson, W.R., 2005. An alternative approach to the SPAC analysis of microtremors: Exploiting stationarity of noise, *Bull. seism. Soc. Am.,* **95**, 277–293.

Cho, I., Tada, T. & Shinozaki, Y., 2006. A generic formulation for microtremor exploration methods using three-component records from a circular array, *Geophys. J. Int.,* **165**(1), 236–259, doi:10.111/j.1365-246X.2006.02880.x.

Chouet, B.A., Dawson, P.B., DeLuca, G., Martini, M., Milana, G., Saccorotti, G. & Scarpa, R., 1998. Array analyses of seismic wavefields radiated by eruptive activity at Stromboli Volcano, Italy, *GNV Spec. Vol., Felici (ed.), Pisa.*

Cornou, C. & Bard, P.Y., 2003. Site-to-bedrock over 1D transfer function ratio: An indicator of the proportion of edge-generated surface waves?, *Geophys. Res. Lett.,* **30**(9), 1453, doi:10.1029/2002GL01659.

DiGiulio, G., Cornou, C., Ohrnberger, M., Wathelet, M. & Rovelli, A., 2006. Deriving wavefield characteristics and shear-velocity profiles from two-dimensional small-apeture array analysis of ambient vibrations in a small-size alluvial basin, Colfiorito, Italy, *Bull. seism. Soc. Am.,* **96**(5), 1915–1933.

Hartzell, S., Leeds, A., Frankel, A. & Michael, J., 1996. Site response for urban Los Angeles using aftershocks of the Northridge earthquake, *Bull. seism. Soc. Am.,* **86**(1b), 168–192.

Haubrich, R.A., 1968. Array Design, *Bull. seism. Soc. Am.,* **58**(3), 977–991.

Herrmann, R.B., 2001. Computer Programs in Seismology, Version 3.1, *St. Louis University.*

Hinzen, K.G., Scherbaum, F. & Weber, B., 2004. On the resolution of H/V measurements to determine sediment thickness, a case study across a normal fault in the Lower Rhine Embayment, Germany, *Journal of Earthquake Engineering,* **8**(6), 909–926.

Horike, M., 1985. Inversion of phase velocity of long-period microtremors to the S wave- velocity structure down to the basement in urbanized areas, *Journal of Physics of the Earth,* **33**(2), 59–96.

Ibs Van Seht, M. & Wohlenberg, J., 1999. Microtremor measurements used to map thickness of soft soil sediments, *Bull. seism. Soc. Am.,* **89**(1), 250–259.

Kvaerna, T. & Ringdahl, F., 1986. Stability of various FK estimation techniques, *Semianual technical summary, 1 October 1985–31 March 1986, NORSAR Scientific Report, Kjeller, Norway,* **1-86/87**, 29–40.

Lachet, C. & Bard, P.Y., 1994. Numerical and theoretical investigations on the possibilities and limitations of Nakamura technique, *Journal of Physics of the Earth,* **42**(5), 377–397.

Lacoss, R.T., Kelly, E.J. & Toksöz, M.N., 1969. Estimation of seismic noise structure using arrays, *Geophysics,* **34**(1), 21–38.

Malagnini, L., Herrmann, R.B., Biella, G. & DeFranco, R., 1995. Rayleigh waves in quaternary alluvium from explosive sources: determination of shear wave velocity and Q structure, *Bull. seism. Soc. Am.,* **85**(3), 900–922.

Menke, W., 1989. Geophysical data analysis: Discrete inverse theory, *Academic Press,* **ISBN 0-12-490921-3**.

Métaxian, J.P., Lesage, P. & Dorel, J., 1997. Permanent tremor of Masaya Volcano, Nicaragua: Wave field analysis and source location, *J. geophys. Res.,* **102**(B10), 22 529–22 546.

Milana, G., Barba, S., DelPezzo, E. & Zambonelli, E., 1996. Site response from ambient noise measurements: New perspectives from an array study in Central Italy, *Bull. seism. Soc. Am.,* **86**(2), 320–328.

Morikawa, H., Sawada, S. & Akamatsu, J., 2004. A method to estimate phase velocities of Rayleigh waves using microseisms simultaneously observed at two sites, *Bull. seism. Soc. Am.,* **94**(3), 961–976.

Ohmachi, T. & Umezono, T., 1998. Rate of rayleigh waves in microtremors, in *Second Int. Symposium on the Effects of Surface Geology on Seismic Motion,* Vol. 2, pp. 587–592, eds Irikura, K., Kudo, K., Okada, H. & Sasatani, T.

Ohori, M., Nobata, A. & Wakamatsu, K., 2002. A comparison of ESAC and FK methods of estimating phase velocity using arbitrarily shaped microtremor arrays, *Bull. seism. Soc. Am.,* **92**(6), 2323–2332.

Ohrnberger, M., Scherbaum, F., Krüger, F., Pelzing, R. & Reamer, S.K., 2004a. How good are shear wave velocity models obtained from inversion of ambient vibrations in the Lower Rhine Embayment (NW-Germany), *Bollettino di Geofisica Teorica ed Applicata,* **45**(3), 215–232.

Ohrnberger, M., Schissele, E., Cornou, C., Wathelet, M., Savvaidis, A., Scherbaum, F., Jongmans, D. & Kind, F., 2004b. Microtremor array measurements for site effect investigations: Comparison of analysis methods for field data crosschecked by simulated wavefields, *13th World Conference on Earthquake Engineering, Vancouver, August 2004,* **paper No. 0940**.

Okada, H., 2003. The Microseismic Survey Method: Society of Exploration Geophysicists of Japan, Translated by Koya Suto, *Geophysical Monograph Series No. 12, Society of Exploration Geophysicists.*

Parolai, S., Bormann, P. & Milkert, C., 2002. New relationships between Vs, thickness of sediments, and resonance frequency calculated by the H/V ratio of seismic noise for Cologne Area (Germany), *Bull. seism. Soc. Am.,* **92**(6), 2521–2527.

Parolai, S., Picozzi, M., Richwalski, S.M. & Milkereit, C., 2005. Joint inversion of phase velocity dispersion and H/V ratio curves from seismic noise recordings using a genetic algorithm, considering higher modes, *Geophys. Res. Lett.,* **32**(1), L01303, doi:10.1029/2004GL021115.

Picozzi, M., Parolai, S. & Richwalski, S.M., 2005. Joint inversion of H/V ratios and dispersion curves from seismic noise: Estimating the S-wave velocity of bedrock, *Geophys. Res. Lett.,* **32**(11), L11308, doi:10.1029/2005GL022878.

Saccorotti, G., Chouet, B. & Dawson, P., 2003. Shallow-velocity models at the Kileau Volcano, Hawai, determined from array analysis of tremor wavefields, *Geophys. J. Int.,* **152**(3), 633–648, doi:10.1046/j.1365-246X.2003.01867.x.

Sambridge, M., 1999a. Geophysical inversion with a neighbourhood algorithm I. Searching a parameter space, *Geophys. J. Int.,* **138**(2), 479–494.

Sambridge, M., 1999b. Geophysical inversion with a neighbourhood algorithm II. Appraising the ensemble, *Geophys. J. Int.,* **138**(3), 727–746.

Scherbaum, F., Hinzen, K.G. & Ohrnberger, M., 2003. Determination of shallow shear wave velocity profiles in the Cologne, Germany area using ambient vibrations, *Geophys. J. Int.,* **152**(3), 597–612.

796   *A. Köhler* et al.

SESAME, 2005. Report on FK/SPAC Capabilities and Limitations, WP06 — Derivation of dispersion curves, *SESAME-Project, EVG1-CT-2000-00026,* **Report-Nr.: D19.06**, http://sesame-fp5.obs.ujf-grenoble.fr.

Shapiro, N.M., Campillo, M., Stehly, L. & Ritzwoller, M.H., 2005. High-resolution surface-wave tomography from ambient seismic noise, *Science,* **307,** 1615–1618.

Tokimatsu, K., 1997. Geotechnical site characterization using surface waves, in *Proc. IS-Tokyo 1995/1st Intl. Conf. Earthquake Geotech. Eng.,* Tokyo, Japan, 14–16 November, **3,** 1333–1368.

Tokimatsu, K. & Miyadera, Y., 1992. Characteristics of rayleigh waves in microtremors and their relation to shear structures, *J. Struct. Constr. Engng, AIJ,* **439,** 81–87, in Japanese.

Wathelet, M., Jongmans, D. & Ohrnberger, M., 2005. Direct inversion of spatial auto-correlation with the neighbourhood algorithm, *Bull. seism. Soc. Am.,* **95**(5), 1787–1800, doi:10.1785/0120040220.

Yamanaka, H., 1998. Geophysical explorations of sedimentary structures and their characterization, in *Second Int. Symposium on the Effects of Surface Geology on Seismic Motion,* Vol. 1, pp. 15–33, eds Irikura, K., Kudo, K., Okada, H. & Sasatani, T.